Commun. Comput. Phys.
doi: 10.4208/cicp.081214.240515s

Vol. **x**, No. x, pp. 1-26
x 2015

Simulation of Incompressible Free Surface Flow Using the Volume Preserving Level Set Method

Ching-Hao Yu[1] and Tony Wen-Hann Sheu[2,3,4,*]

[1] *Department of Ocean Science and Engineering, Zhejiang University, Yuhangtang Road, Hangzhou, Zhejiang, P.R. China.*
[2] *Department of Engineering Science and Ocean Engineering, National Taiwan University, No. 1, Sec. 4, Roosevelt Road, Taipei, Taiwan.*
[3] *Institute of Applied Mathematical Sciences, National Taiwan University, Taiwan.*
[4] *Center of Advanced Study in Theoretical Sciences (CASTS), National Taiwan University, Taiwan.*

Received xxx; Accepted (in revised version) xxx

Abstract. This study aims to develop a numerical scheme in collocated Cartesian grids to solve the level set equation together with the incompressible two-phase flow equations. A seventh-order accurate upwinding combined compact difference (UCCD7) scheme has been developed for the approximation of the first-order spatial derivative terms shown in the level set equation. Developed scheme has a higher accuracy with a three-point grid stencil to minimize phase error. To preserve the mass of each phase all the time, the temporal derivative term in the level set equation is approximated by the sixth-order accurate symplectic Runge-Kutta (SRK6) scheme. All the simulated results for the dam-break, Rayleigh-Taylor instability, bubble rising, two-bubble merging, and milkcrown problems in two and three dimensions agree well with the available numerical or experimental results.

AMS subject classifications: 35Q30, 76D05, 76D27, 76M20

Key words: Level set equation, upwinding combined compact difference scheme, three-point grid stencil, minimize phase error, symplectic Runge-Kutta.

1 Introduction

It is computationally difficult to predict flow equations subject to a sharply varying interface between the air and water. Interface tracking methods encounter deformed meshes that conform to the interface in the Lagrangian sense. The meshes should, as a result, explicitly adapt to the interface. In interface capturing methods, interface is an implicit

*Corresponding author. *Email address:* twhsheu@ntu.edu.tw (T. W.-H. Sheu)

function defined in a fixed mesh. The advantages and disadvantages of applying the Lagrangian type of interface tracking and the Eulerian type of interface capturing methods have been reported in the literature. However, it is still difficult to conclude which methodology is superior to the other.

ALE (Arbitrary Lagrangian Eulerian) [1] method has been well known to be very efficient in modeling a small interface deformation. When interface undergoes a large deformation, a computationally very expensive re-meshing procedure is needed. Boundary integral methods [2–4] were developed to discretize equations along only the interface that separates different liquids, making this class of methods a very attractive one. However, every time when an interface has been merged or split, a time consuming effort is inevitable to continue the computation using the boundary integral method.

The Eulerian based methods in [5–12] are also applicable to the problems having not only a complicated interface but also to the problems involving physical complexities. The VOF method normally involves using a color function and has the ability of conserving the volume of each fluid phase more exactly. The other successful approach developed to model two-phase flows is known as the level set method [13, 14]. The level set function described by Sussman, Smereka and Osher [15] can be easily transported and accurately calculated, respectively. Choice of a proper signed distance function for the sake of re-shaping level set function and implementing re-initialization procedure for the purpose of enhancing numerical stability are normally required while applying level set methods [16].

Level set method applied to simulate interface is known to have the problem regarding the numerical dissipation and mass conservation. Many attempts have been made to circumvent these difficulties [17]. Among them, one can straightforwardly improve the accuracy of the level set solution by the high-order discontinuous Galerkin method [16]. For improving the mass conservation property of the level set method, one can also apply hybrid methods. This class of methods, such as the coupled level set volume of fluid (CLSVOF) method [18] and the particle level set (PLS) method [17], combines an accurate Lagrangian tracking method with the level set method [19]. It is also numerically possible to optimize the level set method by the spatially adaptive method [19] to improve mass conservation. Different adaptive mesh refinements have been conducted to improve the predicted level set solution near the interface considerably, thereby improving the degree of mass conservation. The other method known as the conservative level set method [20] solves the level set equation in conservative form. This method introduces Heaviside function to get a sharp interface approximation. Smearing of the solution with time can be avoided by applying nonlinear re-initialization equation in the simulation of level set equation. For an overview of the level set methods, one can refer to [21–25].

In this paper, a seventh-order upwinding combined compact difference scheme (UCCD7) with the smallest numerical phase error is developed for reducing the dispersion error generated from the discrepancy between the effective and actual scaled wavenumbers. This scheme can predict interface excellently and avoid mass accumulation or depletion. This paper is organized as follows. Section 2 describes the method for

the simulation of two-phase flow system which couples the Navier-Stokes equations with the level set equation. In Section 3, the numerical methods developed for the level set and Navier-Stokes equations are described. Section 4 is devoted to the dispersion analysis of the proposed UCCD7 scheme. The computer code is verified in Section 5 by solving the level set equation subjected to sharply varying flow conditions. Section 6 presents the predicted results for the problems of dam-break, Rayleigh-Taylor instability, bubble rising, two-bubble merging, and droplet falling in water. Finally, some conclusions are drawn in Section 7.

2 Governing equations

2.1 Free surface equation

In this study the level set method is applied to predict the time-varying interface (or free surface) in the two-phase flow domain. At a surface identified to have the zero level set value, i.e. $\phi(\underline{x},t)=0$, both kinematic and dynamic boundary conditions are specified. The kinematic boundary condition is interpreted in the Lagrangian sense, implying that fluid particles on a surface stay always on that surface. We can therefore mathematically express this condition by the advection equation given below for the level set function ϕ whose value is zero at the free surface

$$\phi_t+\underline{u}\cdot\nabla\phi=0. \tag{2.1}$$

The vector $\underline{u}$ denotes the flow velocity.

The level set function ϕ is initially prescribed to have the signed distance values, which are (i) $\phi=-d$ for $x\in\Omega_{gas}$, (ii) $\phi=0$ for $x\in\Gamma_{free\ \ surface}$, and (iii) $\phi=d$ for $x\in\Omega_{liquid}$, in gas and liquid domains. Here, d denotes the absolute normal distance to the interface. Over a time step Δt, the value of ϕ will be computed from Eq. (2.1). The solution computed from this equation is then employed as the initial solution to solve the following re-initialization equation so that ϕ can be always kept as a distance function

$$\phi_\tau+\text{sgn}(\phi_0)(|\nabla\phi|-1)=\lambda\delta(\phi)|\nabla\phi|. \tag{2.2}$$

In the above, $\text{sgn}(\phi_0)=2(H^*(\phi_0)-\frac{1}{2})$ and the smoothed Heaviside function H^* is given below

$$H^*(\phi)=\begin{cases} 0; & \text{if } \phi<-\epsilon, \\ \frac{1}{2}[1+\frac{\phi}{\epsilon}+\frac{1}{\pi}\sin(\frac{\pi\phi}{\epsilon})]; & \text{if } |\phi|\le\epsilon, \\ 1; & \text{if } \phi>\epsilon. \end{cases} \tag{2.3}$$

The Dirac delta function $\delta(\phi)$ shown in (2.2) is approximated by

$$\delta(\phi)=\begin{cases} 0; & \text{if } |\phi|>\epsilon, \\ \frac{1}{2\epsilon}[1+\cos(\frac{\pi\phi}{\epsilon})]; & \text{if } |\phi|\le\epsilon. \end{cases} \tag{2.4}$$

It is noted that in all calculations, ϵ is chosen as $2\Delta x$. To conserve the area bounded by the fluid interface, the parameter λ shown in Eq. (2.2) is prescribed as [22]

$$\lambda = -\frac{\int_{\Omega_{i,j}} \delta(\phi)(-\text{sgn}(\phi_0)(|\nabla\phi|-1))\ d\Omega}{\int_{\Omega_{i,j}} \delta^2(\phi)|\nabla\phi|\ d\Omega}\ . \tag{2.5}$$

2.2 Navier-Stokes equations and fluid property representation

In the present investigation, the liquid and gas are both assumed to be incompressible and immiscible. The resulting equations of motion for these fluid flows can be represented by the following dimensionless incompressible Navier-Stokes equations

$$\underline{u}_t + (\underline{u}\cdot\nabla)\underline{u} = \frac{1}{\rho(\phi)}\Big[-\nabla p + \frac{1}{Re}\nabla\cdot(2\mu(\phi)\underline{\underline{D}}) - \frac{1}{We}\delta(\phi)\kappa(\phi)\nabla\phi\Big] + \frac{1}{Fr^2}\bar{e}_g, \tag{2.6}$$

$$\nabla\cdot\underline{u} = 0. \tag{2.7}$$

Eq. (2.6) involves the Dirac delta function δ, level set function ϕ, and the dimensionless Reynolds number Re $(=\rho_r u_r l_r/\mu_r)$, Froude number Fr $(=u_r/\sqrt{g l_r})$, and Weber numbers We $(=\rho_r u_r^2 l_r/\sigma)$. In the above, σ is the surface tension coefficient and u_r,l_r,ρ_r,μ_r are the referenced values for the respective velocity, length, density and viscosity. The tensor $\underline{\underline{\mathbf{D}}}(=\frac{1}{2}(\nabla\underline{u}+\nabla\underline{u}^{\mathbf{T}}))$ denotes the rate of deformation. The curvature can be represented in terms of the level set function as $\kappa(\phi) = \nabla\cdot\frac{\nabla\phi}{|\nabla\phi|}$.

Across an interface, the smoothed Heaviside function is employed to smooth out the jumps of density and viscosity in the transition zone of $|\phi| \le \epsilon$ so as to avoid numerical instability. In this study, both density and viscosity are assumed to be varied smoothly across the interface by the smoothed Heaviside function $H^*(\phi)$, thereby leading to $\rho(\phi) = \rho_L + (\rho_L - \rho_G)\ H^*(\phi)$ and $\mu(\phi) = \mu_L + (\mu_L - \mu_G)\ H^*(\phi)$. The subscripts G and L shown above represent the gas and liquid phases, respectively.

3 Numerical methods

3.1 Discretization of the level set equation

Under the constant-flow condition, Eq. (2.1) is known to have the Hamiltonian $H = \frac{1}{2}\int_\Omega\ \psi\ \phi\ d\Omega$ [26–28]. For the two-dimensional flow problem, the streamfunction ψ is defined by $u = \frac{\partial\psi}{\partial y}$ and $v = -\frac{\partial\psi}{\partial x}$. Define the function $V_c = \int_{\phi_{i,j,k}\ge c}\ 1\ \ d\Omega$, the area/volume enclosed by the line/surface with the zero contour value of c remains unchanged all the time [28]. In other words, the area/volume within each contour value of ϕ is conserved. Since the inviscid Euler equation belongs to the Hamiltonian class of differential equations [28], the volume preservation property holds. Employment of a scheme accommodating the distinguished area/volume-preserving property is, in particular, essential

when applying the level set method to solve the two-phase flow equations [15]. More precisely, if this intrinsic property is numerically satisfied, the computed volume (for the three-dimensional flow) or area (for the two-dimensional flow) for each fluid flow remains unchanged all the time.

3.1.1 Combined compact difference (UCCD7) scheme for the first-order spatial derivative term

In the following the combined compact difference scheme developed for the approximation of the spatial derivative term ϕ_x, where $\phi=u$ or v, will be presented. Three derivative terms ϕ_x, ϕ_{xx} and ϕ_{xxx} are all considered as the unknown variables at each grid point so as to get the spectral-like resolution. The non-centered combined compact difference scheme developed in a three-point grid stencil for the approximation of the derivative terms $\frac{\partial\phi}{\partial x}$, $\frac{\partial^2\phi}{\partial x^2}$ and $\frac{\partial^3\phi}{\partial x^3}$ is as follows

$$\begin{aligned}
&\frac{\partial\phi}{\partial x}|_i+a_1\frac{\partial\phi}{\partial x}|_{i-1}+h\left(b_1\frac{\partial^2\phi}{\partial x^2}|_{i-1}+b_2\frac{\partial^2\phi}{\partial x^2}|_i+b_3\frac{\partial^2\phi}{\partial x^2}|_{i+1}\right)\\
&\quad+h^2\left(c_1\frac{\partial^3\phi}{\partial x^3}|_{i-1}+c_3\frac{\partial^3\phi}{\partial x^3}|_{i+1}\right)=\frac{1}{h}(d_1\phi_{i-1}+d_2\phi_i+d_3\phi_{i+1}), \qquad (3.1)\\
&\frac{\partial^2\phi}{\partial x^2}|_i+\frac{29}{16h}(-\frac{\partial\phi}{\partial x}|_{i-1}+\frac{\partial\phi}{\partial x}|_{i+1})+\frac{5}{16}\left(-\frac{\partial^2\phi}{\partial x^2}|_{i-1}-\frac{\partial^2\phi}{\partial x^2}|_{i+1}\right)\\
&\quad+\frac{h}{48}\left(-\frac{\partial^3\phi}{\partial x^3}|_{i-1}+\frac{\partial^3\phi}{\partial x^3}|_{i+1}\right)=\frac{4}{h^2}(\phi_{i-1}-2\phi_i+\phi_{i+1}), \qquad (3.2)\\
&\frac{\partial^3\phi}{\partial x^3}|_i+\frac{105}{16h^2}(-\frac{\partial\phi}{\partial x}|_{i-1}-\frac{\partial\phi}{\partial x}|_{i+1})+\frac{15}{8h}\left(-\frac{\partial^2\phi}{\partial x^2}|_{i-1}+\frac{15}{8}\frac{\partial^2\phi}{\partial x^2}|_{i+1}\right)\\
&\quad+\frac{3}{16}\left(-\frac{\partial^3\phi}{\partial x^3}|_{i-1}-\frac{\partial^3\phi}{\partial x^3}|_{i+1}\right)=\frac{105}{16h^3}(\phi_{i-1}-\phi_{i+1}). \qquad (3.3)
\end{aligned}$$

In the above, the second-order derivative term $\frac{\partial^2\phi}{\partial x^2}$ and the third-order derivative term $\frac{\partial^3\phi}{\partial x^3}$ are approximated by centered schemes. The coefficients in (3.2) and (3.3) are determined by the method of Taylor series expansions. By eliminating the leading truncation error terms in the derived modified equations, the resulting formal accuracy orders for ϕ_{xx} and ϕ_{xxx} become eight and six, respectively.

For the description of the proposed upwinding compact difference scheme $\frac{\partial\phi}{\partial x}$, in the following we present only the positive-valued velocity case. The coefficients for the case involving a negative velocity can be similarly derived. Determination of the weighting coefficients in (3.1) is started by applying the Taylor series expansion for the terms ϕ_{i-1}, ϕ_{i+1}, $\frac{\partial\phi}{\partial x}|_{i-1}$, $\frac{\partial\phi}{\partial x}|_i$, $\frac{\partial^2\phi}{\partial x^2}|_{i-1}$, $\frac{\partial^2\phi}{\partial x^2}|_i$, $\frac{\partial^2\phi}{\partial x^2}|_{i+1}$, $\frac{\partial^3\phi}{\partial x^3}|_{i-1}$ and $\frac{\partial^3\phi}{\partial x^3}|_{i+1}$ with respect to the term ϕ_i. Let the leading eight error terms shown in the derived modified equation for $\frac{\partial\phi}{\partial x}$ to be zero,

the following set of algebraic equations can be derived

$$d_1+d_2+d_3=0, \tag{3.4}$$
$$-a_1-d_1+d_3=1, \tag{3.5}$$
$$2a_1+d_1+d_3-2b_1-2b_2-2b_3=0, \tag{3.6}$$
$$d_1-d_3-6b_1+6b_3+6c_1+6c_3+3a_1=0, \tag{3.7}$$
$$d_1+d_3-12b_1-12b_3+24c_1-24c_3+4a_1=0, \tag{3.8}$$
$$d_1-d_3-20b_1+20b_3+60c_1+60c_3+5a_1=0, \tag{3.9}$$
$$d_1+d_3-30b_1-30b_3+120c_1-120c_3+6a_1=0, \tag{3.10}$$
$$d_1-d_3-42b_1+42b_3+210c_1+210c_3+7a_1=0. \tag{3.11}$$

Since the investigated level set equation accounts for the wave-like free surface, the weighting coefficients in (3.1) determined solely from the above truncation error analysis (or modified equation analysis) are inadequate to fully exhibit wave characteristics. To this end, Fourier method of error analysis is employed to quantify the dispersive numerical error and the resolution characteristics in association with Eq. (3.1) by matching the numerical modified (or scaled) wavenumber with its analytical counterpart [29]. When implementing the Fourier transform on (3.1), the Fourier transform $\tilde{\phi}(\alpha)=\frac{1}{2\pi}\int_{-\infty}^{+\infty}\phi(x)\ e^{-\mathbf{i}\alpha x}\ dx$ and its inverse for ϕ_x, namely, $\phi(x)=\int_{-\infty}^{+\infty}\tilde{\phi}(\alpha)\ e^{\mathbf{i}\alpha x}\ d\alpha$ are employed. Note that the notation $\mathbf{i}$ shown above equals to $\sqrt{-1}$.

By performing the Fourier transform on each term shown in Eqs. (3.1), (3.2) and (3.3), we can get the expressions of the actual (or exact) wavenumber α as follows

$$\begin{aligned}
&\mathbf{i}\alpha h\ (a_1\exp(-\mathbf{i}\alpha h)+1)\\
\simeq& d_1\exp(-\mathbf{i}\alpha h)+d_2+d_3\exp(\mathbf{i}\alpha h)-(\mathbf{i}\alpha h)^2(b_1\exp(-\mathbf{i}\alpha h)+b_2+b_3\exp(\mathbf{i}\alpha h))\\
&-(\mathbf{i}\alpha h)^3(c_1\exp(-\mathbf{i}\alpha h)+c_3\exp(\mathbf{i}\alpha h)),
\end{aligned} \tag{3.12}$$

$$\begin{aligned}
&\frac{29}{16}\mathbf{i}\alpha h\ (-\exp(-\mathbf{i}\alpha h)+\exp(\mathbf{i}\alpha h))\\
\simeq& 4(\exp(-\mathbf{i}\alpha h)-2+\exp(\mathbf{i}\alpha h))-(\mathbf{i}\alpha h)^2\Big(-\frac{5}{16}\exp(-\mathbf{i}\alpha h)+1-\frac{5}{16}\exp(\mathbf{i}\alpha h)\Big)\\
&-\frac{1}{48}(\mathbf{i}\alpha h)^3(-\exp(-\mathbf{i}\alpha h)+\exp(\mathbf{i}\alpha h)),
\end{aligned} \tag{3.13}$$

$$\begin{aligned}
&\frac{105}{16}\mathbf{i}\alpha h\ (-\exp(-\mathbf{i}\alpha h)-\exp(\mathbf{i}\alpha h))\\
\simeq&\frac{105}{16}(\exp(-\mathbf{i}\alpha h)-\exp(\mathbf{i}\alpha h))-\frac{15}{8}(\mathbf{i}\alpha h)^2(-\exp(-\mathbf{i}\alpha h)+\exp(\mathbf{i}\alpha h))\\
&-(\mathbf{i}\alpha h)^3\Big(-\frac{3}{16}\exp(-\mathbf{i}\alpha h)+1-\frac{3}{16}\exp(\mathbf{i}\alpha h)\Big).
\end{aligned} \tag{3.14}$$

When solving hydrodynamic or wave equations, it is desired that the effective (or numerical) scaled wavenumbers $\alpha' h$, $\alpha'' h$ and $\alpha''' h$ have almost the same expressions as those

shown in the right-hand sides of Eqs. (3.12), (3.13) and (3.14) [29]. We can, as a result, express $\alpha' h$, $\alpha'' h$ and $\alpha''' h$ as follows

$$\begin{aligned}
&\mathbf{i}\alpha' h\,(a_1\exp(-\mathbf{i}\alpha h)+1)\\
=&d_1\exp(-\mathbf{i}\alpha h)+d_2+d_3\exp(\mathbf{i}\alpha h)-(\mathbf{i}\alpha'' h)^2(b_1\exp(-\mathbf{i}\alpha h)+b_2+b_3\exp(\mathbf{i}\alpha h))\\
&-(\mathbf{i}\alpha''' h)^3(c_1\exp(-\mathbf{i}\alpha h)+c_3\exp(\mathbf{i}\alpha h)), \qquad (3.15)\\
&\frac{29}{16}\mathbf{i}\alpha' h\,(-\exp(-\mathbf{i}\alpha h)+\exp(\mathbf{i}\alpha h))\\
=&4(\exp(-\mathbf{i}\alpha h)-2+\exp(\mathbf{i}\alpha h))-(\mathbf{i}\alpha'' h)^2\Big(-\frac{5}{16}\exp(-\mathbf{i}\alpha h)+1-\frac{5}{16}\exp(\mathbf{i}\alpha h)\Big)\\
&-\frac{1}{48}(\mathbf{i}\alpha''' h)^3(-\exp(-\mathbf{i}\alpha h)+\exp(\mathbf{i}\alpha h)), \qquad (3.16)\\
&\frac{105}{16}\mathbf{i}\alpha' h\,(-\exp(-\mathbf{i}\alpha h)-\exp(\mathbf{i}\alpha h))\\
=&\frac{105}{16}(\exp(-\mathbf{i}\alpha h)-\exp(\mathbf{i}\alpha h))-\frac{15}{8}(\mathbf{i}\alpha'' h)^2(-\exp(-\mathbf{i}\alpha h)+\exp(\mathbf{i}\alpha h))\\
&-(\mathbf{i}\alpha''' h)^3\Big(-\frac{3}{16}\exp(-\mathbf{i}\alpha h)+1-\frac{3}{16}\exp(\mathbf{i}\alpha h)\Big). \qquad (3.17)
\end{aligned}$$

By solving Eqs. (3.15), (3.16) and (3.17) altogether, $\alpha' h$ can be derived in a complex function form.

The real and imaginary parts of the numerical modified (or scaled) wavenumber $\alpha' h$ account respectively for the numerically generated dispersion error (phase error) and the dissipation error (amplitude error). For the purpose of getting a better predicted dispersive accuracy for α', we demand that $\alpha h \approx \Re[\alpha' h]$, where $\Re[\alpha' h]$ denotes the real part of $\alpha' h$, and the magnitude of $E(\alpha)$ defined below be very small and positive

$$E(\alpha)=\int_{-\frac{\pi}{2}}^{\frac{\pi}{2}}\left[W\left(\alpha h-\Re[\alpha' h]\right)\right]^2 d(\alpha h). \qquad (3.18)$$

For the purpose of analytically integrating $E(\alpha)$, the weighting function W is introduced in (3.18). Unlike the unit weighting function used in the work of Tam and Webb [29], in this study the weighting function W is chosen as the denominator of $(\alpha h-\Re[\alpha' h])$.

To make the error function defined in the full range optimization $-\frac{\pi}{2}\le\alpha h\le\frac{\pi}{2}$ to be a positive and minimum value, the extreme condition $\frac{\partial E}{\partial d_1}=0$ is enforced to minimize the numerical wavenumber error. The equation derived from the Fourier analysis and the eight previously derived algebraic equations aiming at getting a higher dissipation and dispersion accuracy can be used together to compute the nine unknowns in (3.1), which are given as $a_1=1.1875$, $b_1=0.23643236$, $b_2=-0.27774699$, $b_3=-0.01356764$, $c_1=0.01894044$, $c_3=0.00189289$, $d_1=-2.33613227$, $d_2=2.48476453$, $d_3=-0.14863227$. In the grid points $i-1$, i and $i+1$, the proposed scheme is shown to have the spatial accuracy of order seven for $\frac{\partial\phi}{\partial x}$ according to the derived modified equation $\frac{\partial\phi}{\partial x}=\frac{\partial\phi}{\partial x}|_{exact}-0.65175737\times$

$10^{-5}\ h^7\frac{\partial^8\phi}{\partial x^8}+0.816532935\times10^{-7}\ h^9\frac{\partial^{10}\phi}{\partial x^{10}}+H.O.T.$. When $u<0$, the proposed non-centered combined compact difference scheme can be similarly derived below for the derivative term $\frac{\partial\phi}{\partial x}$

$$\begin{aligned}&\frac{\partial\phi}{\partial x}|_i+1.1875\frac{\partial\phi}{\partial x}|_{i+1}+h\left(0.013567\frac{\partial^2\phi}{\partial x^2}|_{i-1}+0.277746\frac{\partial^2\phi}{\partial x^2}|_i-0.236432\frac{\partial^2\phi}{\partial x^2}|_{i+1}\right)\\&\quad+h^2\left(0.001892\frac{\partial^3\phi}{\partial x^3}|_{i-1}+0.018940\frac{\partial^3\phi}{\partial x^3}|_{i+1}\right)\\&=\frac{1}{h}(0.148632\phi_{i-1}-2.484764\phi_i+2.336132\phi_{i+1}).\end{aligned}\tag{3.19}$$

3.1.2 Symplectic Runge-Kutta (SRK6) scheme for the temporal derivative term

For retaining the long-time accurate Hamiltonian and volume-preserving properties existing in Eq. (2.1), the time derivative term will be discretized by the structure-preserving scheme. In this paper, the sixth-order temporally accurate symplectic Runge-Kutta scheme [30] is employed to solve the ordinary differential equation $\frac{d\phi}{dt}=F(\phi)$.

Given the solution ϕ^n at $t=n\Delta t$, calculation of the solution ϕ^{n+1} starts from the guessed values $\phi^{(i)}$ for ϕ^n, where i=1 to 3. The computed values of $F^{(i)}$ ($i=1$ to 3) are then substituted into the three implicit equations given below to get the updated values of $\phi^{(i)}$ (i= 1 to 3)

$$\phi^{(1)}=\phi^n+\Delta t\left[\frac{5}{36}F^{(1)}+\left(\frac{2}{9}+\frac{2\widetilde{c}}{3}\right)F^{(2)}+\left(\frac{5}{36}+\frac{\widetilde{c}}{3}\right)F^{(3)}\right],\tag{3.20}$$

$$\phi^{(2)}=\phi^n+\Delta t\left[\left(\frac{5}{36}-\frac{5\widetilde{c}}{12}\right)F^{(1)}+\frac{2}{9}F^{(2)}+\left(\frac{5}{36}+\frac{5\widetilde{c}}{12}\right)F^{(3)}\right],\tag{3.21}$$

$$\phi^{(3)}=\phi^n+\Delta t\left[\left(\frac{5}{36}-\frac{\widetilde{c}}{3}\right)F^{(1)}+\left(\frac{2}{9}-\frac{2\widetilde{c}}{3}\right)F^{(2)}+\frac{5}{36}F^{(3)}\right],\tag{3.22}$$

where $\widetilde{c}=\frac{1}{2}\sqrt{\frac{3}{5}}$. Note that $F^{(i)}$ (i= 1 to 3) shown above represent the values of $F(\equiv-\underline{u}\cdot\nabla\phi)$ at $t=n+(\frac{1}{2}+\widetilde{c})\Delta t$, $t=n+\frac{1}{2}\Delta t$, and $t=n+(\frac{1}{2}-\widetilde{c})\Delta t$, respectively. As the difference of $\phi^{(i)}$ computed from the two consecutive iterations becomes negligibly small, the solution of ϕ at $t=(n+1)\Delta t$ is obtained as $\phi^{n+1}=\phi^n+\frac{\Delta t}{9}\ [\frac{5}{2}F^{(1)}+4F^{(2)}+\frac{5}{2}F^{(3)}]$.

3.2 Discretization of the re-initialization equation

In the re-initialization equation (2.2) we apply the fifth-order accurate weighted essentially non-oscillatory (WENO5) scheme [31] to approximate the spatial derivative term. As for the temporal derivative term in Eq. (2.2) or $\frac{d\phi}{d\tau}=L(\phi)=-\text{sgn}(\phi_0)(|\nabla\phi|-1)+\lambda\delta(\phi)|\nabla\phi|$, the third-order accurate TVD Runge-Kutta (TVD-RK3) scheme [32] is applied. The solution of the above ordinary differential equation will be sought from the

following solution steps

$$\phi^{(1)}=\phi^{(n)}+\Delta\tau L(\phi^{(0)}), \tag{3.23}$$

$$\phi^{(2)}=\frac{3}{4}\phi^{(n)}+\frac{1}{4}\phi^{(1)}+\frac{1}{4}\Delta\tau L(\phi^{(1)}), \tag{3.24}$$

$$\phi^{(n+1)}=\frac{1}{3}\phi^{(n)}+\frac{2}{3}\phi^{(2)}+\frac{2}{3}\Delta\tau L(\phi^{(2)}). \tag{3.25}$$

3.3 Approximation of the first-order derivative terms in the momentum equations

Approximation of the convective terms in Navier-Stokes equations needs to take the upwinding nodal solutions into a favorable consideration. In this section, a fifth-order accurate upwinding combined compact difference scheme having a better dispersion relation is proposed. Our primary aim is to enhance convective stability by virtue of the increased dispersive accuracy.

The non-centered combined compact difference scheme for $\phi=u$ (or v) has been developed in a three-point grid stencil for the approximation of the first-order derivative terms as follows

$$\begin{aligned}0.875\frac{\partial\phi}{\partial x}|_{i-1}+\frac{\partial\phi}{\partial x}|_i=&\frac{1}{h}(-1.935961\phi_{i-1}+1.996922\phi_i-0.0606961\phi_{i+1})\\&-h\left(0.125128\frac{\partial^2\phi}{\partial x^2}|_{i-1}-0.248717\frac{\partial^2\phi}{\partial x^2}|_i+0.000128\frac{\partial^2\phi}{\partial x^2}|_{i+1}\right),\end{aligned} \tag{3.26}$$

$$-\frac{1}{8}\frac{\partial^2\phi}{\partial x^2}|_{i-1}+\frac{\partial^2\phi}{\partial x^2}|_i-\frac{1}{8}\frac{\partial^2\phi}{\partial x^2}|_{i+1}=\frac{3}{h^2}(\phi_{i-1}-2\phi_i+\phi_{i+1})-\frac{9}{8h}\left(-\frac{\partial\phi}{\partial x}|_{i-1}+\frac{\partial\phi}{\partial x}|_{i+1}\right). \tag{3.27}$$

The above three-point upwinding combined compact difference scheme for $\frac{\partial\phi}{\partial x}$ has been shown to have the spatial accuracy order of five according to the derived modified equation $\frac{\partial\phi}{\partial x}=\frac{\partial\phi}{\partial x}|_{exact}-0.000700856\ h^5\frac{\partial^6\phi}{\partial x^6}+0.00019841\ h^6\frac{\partial^7\phi}{\partial x^7}+H.O.T.$.

3.4 Projection method for the two phase flow equations

Following the idea of projection method given in [33], the predicted pressure p^* is used to calculate the intermediate velocity $\underline{u}^*$, which does not necessarily satisfy the divergence-free constraint condition, from the following vector momentum equation

$$\frac{\underline{u}^*-\underline{u}^n}{\Delta t}+(\underline{u}^*\cdot\nabla)\underline{u}^*-\frac{1}{Re}\frac{\nabla\cdot(2\mu(\phi)\underline{\underline{\mathbf{D}}}^*)}{\rho(\phi)}+\frac{\nabla p^*}{\rho(\phi)}+\underline{f}=0. \tag{3.28}$$

The term $\underline{f}$ shown above is expressed as $\frac{1}{We}\frac{\kappa(\phi)\ \delta(\phi)\ \nabla\phi}{\rho(\phi)}-\frac{1}{Fr^2}\underline{e}_g$. The velocity is then projected to the divergence-free space. The value of pressure is then updated by the equa-

tions given below

$$\frac{\underline{u}^{n+1}-\underline{u}^{*}}{\Delta t}=-\frac{\nabla p'}{\rho(\phi)}, \tag{3.29}$$

$$p^{n+1}=p^{*}+p', \tag{3.30}$$

$$\nabla\cdot\underline{u}^{n+1}=0. \tag{3.31}$$

Substitution of Eq. (3.29) to the semi-discrete equation

$$\frac{\underline{u}^{n+1}-\underline{u}^{n}}{\Delta t}+(\underline{u}^{n+1}\cdot\nabla)\underline{u}^{n+1}-\frac{1}{Re}\frac{\nabla\cdot(2\mu(\phi)\underline{\underline{\mathbf{D}}}^{n+1})}{\rho(\phi)}+\frac{\nabla p^{n+1}}{\rho(\phi)}+\underline{f}=0 \tag{3.32}$$

yields

$$\frac{\underline{u}^{n+1}-\underline{u}^{n}}{\Delta t}+(\underline{u}^{*}\cdot\nabla)\underline{u}^{*}-\frac{1}{Re}\frac{\nabla\cdot(2\mu(\phi)\underline{\underline{\mathbf{D}}}^{*})}{\rho(\phi)}+\frac{\nabla p^{*}}{\rho(\phi)}+\underline{f}=-\frac{\nabla p'}{\rho(\phi)}+M_1+M_2. \tag{3.33}$$

In the above [34],

$$M_1=\left[(\underline{u}^{*}\cdot\nabla)\frac{\nabla p'}{\rho(\phi)}+\Big(\frac{\nabla p'}{\rho(\phi)}\cdot\nabla\Big)\underline{u}^{*}-\frac{1}{Re}\nabla^2\Big(\frac{\nabla p'}{\rho(\phi)}\Big)\right]\Delta t, \tag{3.34}$$

$$M_2=-\left[\Big(\frac{\nabla p'}{\rho(\phi)}\cdot\nabla\Big)\frac{\nabla p'}{\rho(\phi)}\right]\Delta t^2. \tag{3.35}$$

The remaining task of the applied method is to derive the equation for p', which has been derived in detail in [34]

$$p'_{i,j}=p'^{*}_{i,j}+\frac{\frac{p'^{*}_{i-1,j}}{\rho_{i-\frac{1}{2},j}\Delta x^2}+\frac{p'^{*}_{i+1,j}}{\rho_{i+\frac{1}{2},j}\Delta x^2}+\frac{p'^{*}_{i,j-1}}{\rho_{i,j-\frac{1}{2}}\Delta y^2}+\frac{p'^{*}_{i,j+1}}{\rho_{i,j+\frac{1}{2}}\Delta y^2}}{\frac{1}{\rho_{i-\frac{1}{2},j}\Delta x^2}+\frac{1}{\rho_{i+\frac{1}{2},j}\Delta x^2}+\frac{1}{\rho_{i,j-\frac{1}{2}}\Delta y^2}+\frac{1}{\rho_{i,j+\frac{1}{2}}\Delta y^2}}, \tag{3.36}$$

where

$$p'^{*}_{i,j}=-\frac{\nabla\cdot\ \underline{u}^{*}_{i,j}}{\Delta t(\frac{1}{\rho_{i-\frac{1}{2},j}\Delta x^2}+\frac{1}{\rho_{i+\frac{1}{2},j}\Delta x^2}+\frac{1}{\rho_{i,j-\frac{1}{2}}\Delta y^2}+\frac{1}{\rho_{i,j+\frac{1}{2}}\Delta y^2})}. \tag{3.37}$$

4 Fundamental analysis of the proposed scheme

4.1 Assessment of the dispersion and dissipation errors

The solution of the model equation $u_t+c\ u_x=0$ is represented by $u=\hat{u}_\alpha(t)e^{\mathbf{i}\alpha x}$, where $\mathbf{i}\equiv\sqrt{-1}$ and $\hat{u}_\alpha$ is the Fourier mode of the wave number α. Differentiation of this equation

leads to $\frac{\partial u}{\partial x}|_{exact} = \mathbf{i}\alpha h \frac{\hat{u}_\alpha}{h} e^{\mathbf{i}\alpha x}$, where the wavenumber has been scaled by $h = \frac{L}{N}$. Note that L is the length of physical domain and N is the number of grid intervals. The approximated derivative term $\frac{\partial u}{\partial x}$ can be similarly written as

$$\frac{\partial u}{\partial x}|_{numerical} = \mathbf{i}\alpha' h \frac{\hat{u}_\alpha}{h} e^{\mathbf{i}\alpha x} = (K_r + \mathbf{i}K_i)\frac{\hat{u}_\alpha}{h} e^{\mathbf{i}\alpha x}. \tag{4.1}$$

In the above, K_r and K_i denote the real and imaginary parts, respectively. One can express the coefficients K_i and K_r in terms of the real part $(\alpha' h)$ and the imaginary part $(\alpha' h)$ shown respectively in (3.15) as $K_i = \Re[\alpha' h]$ and $K_r = -\Im[\alpha' h]$.

In Fig. 1, the values of K_i and K_r are plotted with respect to the scaled wavenumber αh for the present three-point upwinding combined compact difference scheme UCCD7. One can easily find that the proposed upwind scheme is better than the other schemes [35, 36] owing to the improved dispersive accuracy. The positive-valued K_r calculated from the UCCD7 scheme is, however, less accurate than the non-dissipative (or K_r = 0) centered-type combined compact difference scheme of Nihei and Ishii [35].

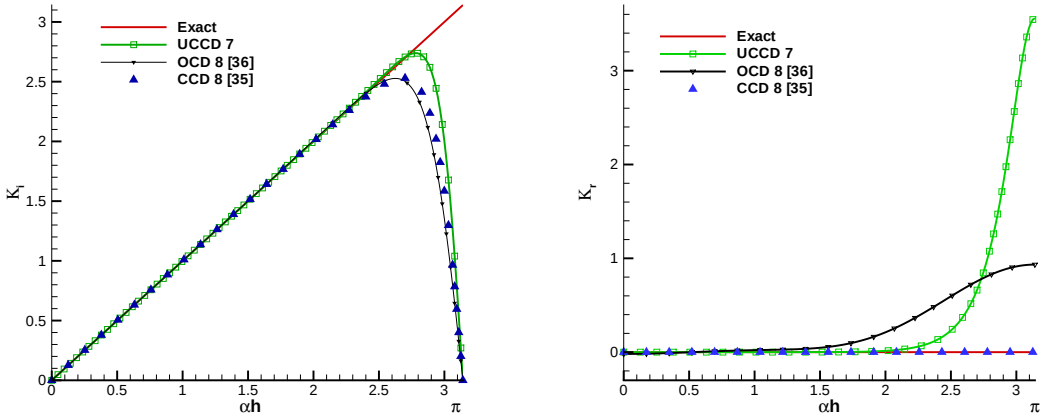

(a) (b)

Figure 1: Comparison of $K_r(\alpha h)$ and $K_i(\alpha h)$ amongst the proposed three-point seventh-order accurate upwinding combined compact difference scheme (UCCD7), seven-point eighth-order accurate optimized centered compact difference scheme (OCD8) [36], and the three-point eighth-order accurate centered combined compact difference scheme (CCD8) [35]. (a) K_i; (b) K_r.

4.2 Assessment of the phase speed anisotropy

The two-dimensional equation $u_t + c_x\ u_x + c_y\ u_y = 0$ is taken into consideration, where $c_x = c\cos(\theta)$ and $c_y = c\sin(\theta)$ denote the velocity components along the x and y directions, respectively. For a wave propagating at the angle θ $(\equiv \tan^{-1}(\frac{c_y}{c_x}))$ with respect to the x-

axis, the numerical phase speed anisotropy can be derived as follows [37–39]

$$\Re\left(\frac{c^*}{c}\right)=\frac{\cos(\theta)\Re[\alpha' h(\alpha h\,\cos(\theta))]+\,\sin(\theta)\Re[\alpha' h(\alpha h\,\sin(\theta))]}{\alpha h}. \tag{4.2}$$

In Fig. 2 one can find that at all the scaled wavenumbers the proposed scheme has a much better phase speed anisotropy than the other schemes.

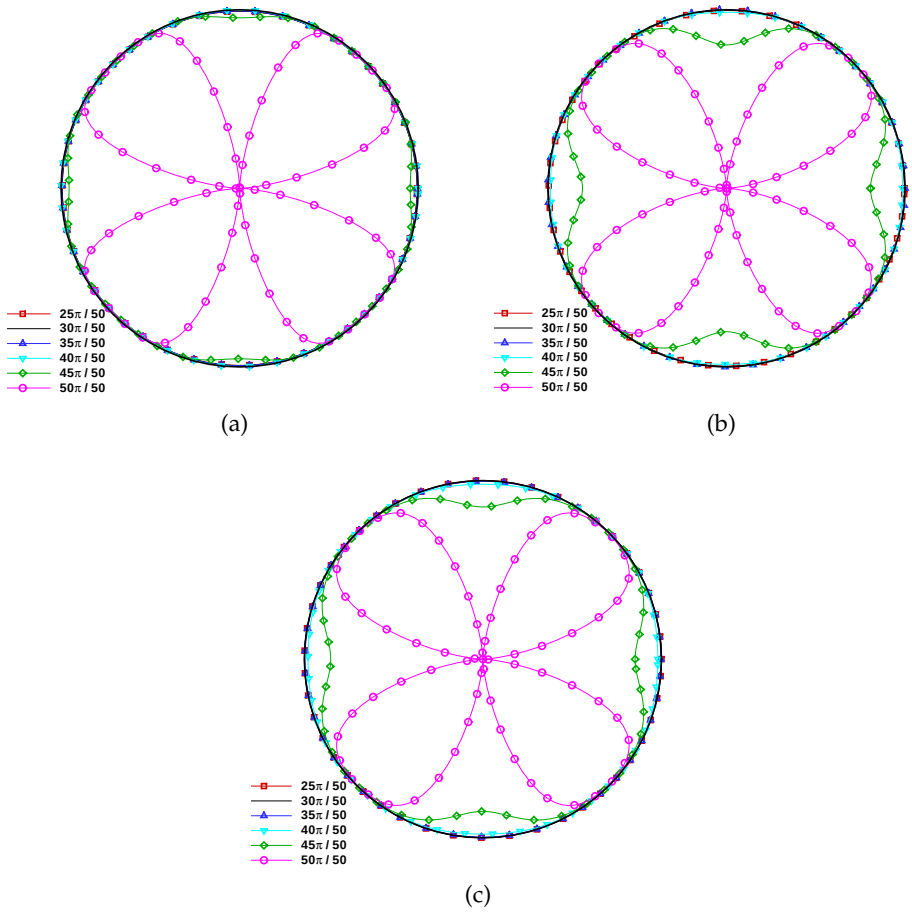

Figure 2: The phase speed anisotropy predicted at different modified wave numbers αh for the proposed and two referenced schemes. (a) UCCD7; (b) OCDS8 [36]; (c) CCD8 [35].

5 Verification studies

The level set method will be verified for the case with the prescribed velocity field. We define below the ratios $N_{c=0}$ and $M_{c=0}$ for measuring the area and volume errors

$$N_{c=0} = \frac{A_0(t)}{A_0(t=0)}, \tag{5.1}$$

$$M_{c=0} = \frac{V_0(t)}{V_0(t=0)}. \tag{5.2}$$

Note that the computed value of A_0 denotes the area for the two dimensional case and the computed value of V_0 represents the volume for the three-dimensional case. The values of A_0 and V_0 are computed by calculating the area or volume enclosed by the contour of the level set function $\phi=0$, respectively.

5.1 Smooth Gaussian problem

To verify the proposed seventh-order spatially accurate upwinding combined compact difference scheme, the problem with the smooth exact solution $\phi=\exp(-\frac{(x+3)^2}{4}-\frac{(y+3)^2}{4})$ for Eq. (2.1) is solved at $u=-\frac{2\pi y}{9}$ and $v=\frac{2\pi x}{9}$ in the square $-1\leq x\leq 1$ and $-1\leq y\leq 1$. The calculation is performed at $\Delta t=\frac{1}{2000}$, which is much smaller than the three chosen grid spacings Δx, which are $\frac{2}{15}$, $\frac{2}{25}$ and $\frac{2}{35}$. The L_2-error norms and their corresponding spatial rates of convergence computed at a time after ten rotations are tabulated in Table 1.

Table 1: The predicted L_2-error norms at $\Delta t=\frac{1}{2000}$ and the corresponding spatial rates of convergence for the solutions predicted after 10 rotations (or at $t=90$) in a domain containing three chosen meshes for the rotation of a smooth Gaussian profile. This problem is described in Section 5.1.

Grids	L_2 error norms	rates of convergence
15×15	2.6332×10^{-2}	
25×25	1.1115×10^{-3}	6.1959
35×35	9.8861×10^{-5}	7.1916

5.2 Slotted (Zalesak's) disk problem

The Zalesak's problem [40] is then solved to verify the developed advection scheme. The slotted disk has a radius of 15 and a slot width of 5. It is initially located at $(50,75)$ in the domain of size $(100,100)$. The prescribed velocity field is given by $(u=\frac{\pi(50-y)}{314}, v=\frac{\pi(x-50)}{314})$. The results predicted in 200×200 mesh points after 200 revolutions are plotted in Fig. 3(a). Our computed solution has also shown good agreement with the exact (or initial) area ratio shown in Fig. 3(b).

5.3 Three-dimensional vortex flow in a cube

The ability of the UCCD7 scheme is then demonstrated by solving the flow problem with the following velocity components $u=\sin^2(\pi x)\sin(2\pi y)\sin(2\pi z)\cos(\frac{\pi t}{T})$, $v=$

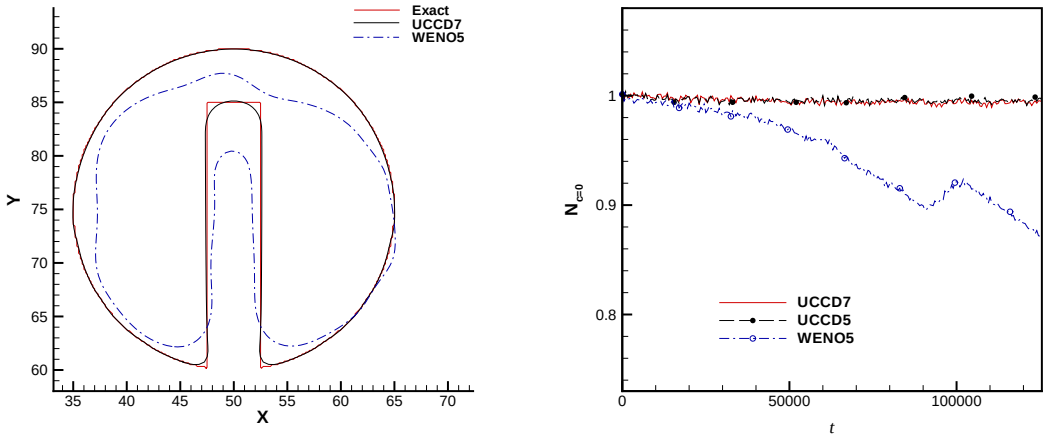

(a) (b)

Figure 3: Comparison of the results for the Zalesak's problem computed in 200×200 grids. (a) after 200 revolutions; (b) Comparison of the predicted area ratios, defined in (5.1), versus time t for the calculations carried out in 200×200 grids.

$-\sin(2\pi x)\sin^2(\pi y)\sin(2\pi z)\cos(\frac{\pi t}{T})$, $w=-\sin(2\pi x)\sin(2\pi y)\sin^2(\pi z)\cos(\frac{\pi t}{T})$ at $T=3$. A sphere of the radius 0.15 is placed in a unit cube centered at $(0.35,0.35,0.35)$. This sphere is stretched by the prescribed vortex flow, thereby scooping out the sphere. Afterwards, it reverses back to the initial shape. The results computed in $150\times150\times150$ mesh points look like the results of Wang et al. [41] shown in Fig. 4. The relative mass errors tabulated in Table 2 show the increasingly larger error.

Table 2: Comparison of the computed percentages of the total mass error. Note that LS means the level set method.

methods Grids	LS [41] 100^3	present LS 100^3	present LS 150^3
$t=1.5$	21.8%	2.21%	1.2%
$t=3.0$	32.1%	4.47%	2.5%

6 Numerical results

After verifying the advection scheme, the proposed level set method is validated by solving the following five incompressible Navier-Stokes problems, which all involve the time-varying interfaces.

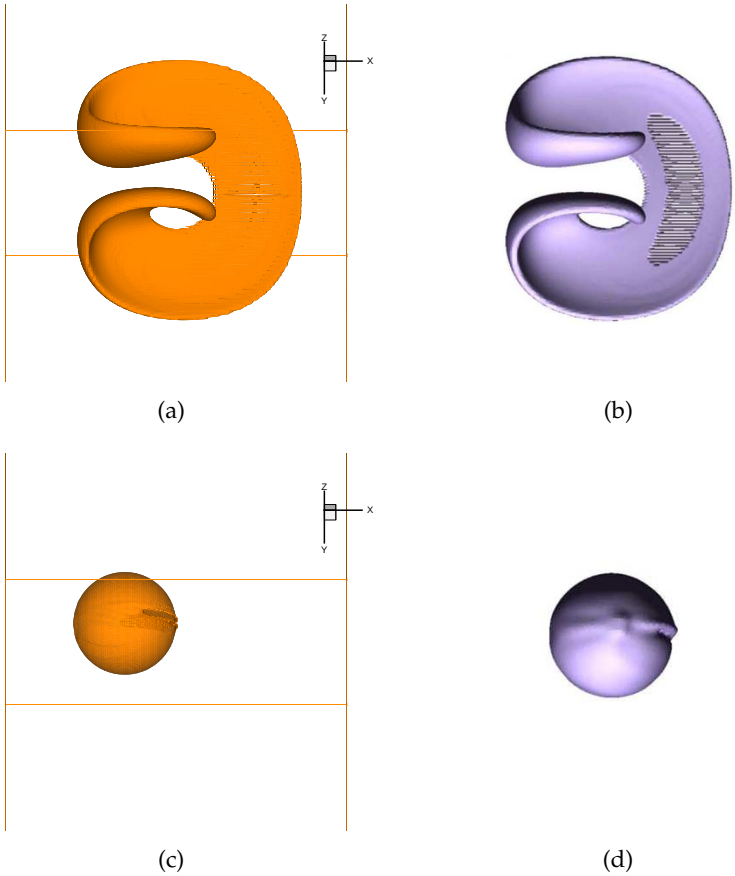

Figure 4: Simulation of a deformed sphere in $150\times150\times150$ grids. (a) UCCD7 solution at $t=1.5$; (b) reference solution at $t=1.5$ [41]; (c) UCCD7 solution at $t=3.0$; (d) reference solution at $t=3.0$ [41].

6.1 Interface prediction without surface tension

6.1.1 Dam break problem

A tank of the area $4a\times2.4a$ and a water column of the area $a\times2a$ are considered at $a=0.146m$. No-slip boundary conditions are imposed on the walls of the investigated tank. The water density under investigation is $\rho_w=1000\frac{kg}{m^3}$ and its dynamic viscosity is $\mu_w=0.001\frac{kg}{ms}$. The air density is $\rho_a=1\frac{kg}{m^3}$ and the dynamic viscosity is $\mu_a=0.0001\frac{kg}{ms}$.

In Fig. 5(a), the numerical results predicted in 400×240 grids are presented. The area ratio $N_{c=0}$ is shown in Fig. 5(b), from which the mass is seen to lose by an amount less than 0.5%. Good agreement with the numerical and experimental results given in [42–44] is also clearly demonstrated in Fig. 6 for the surge front location and the water column height.

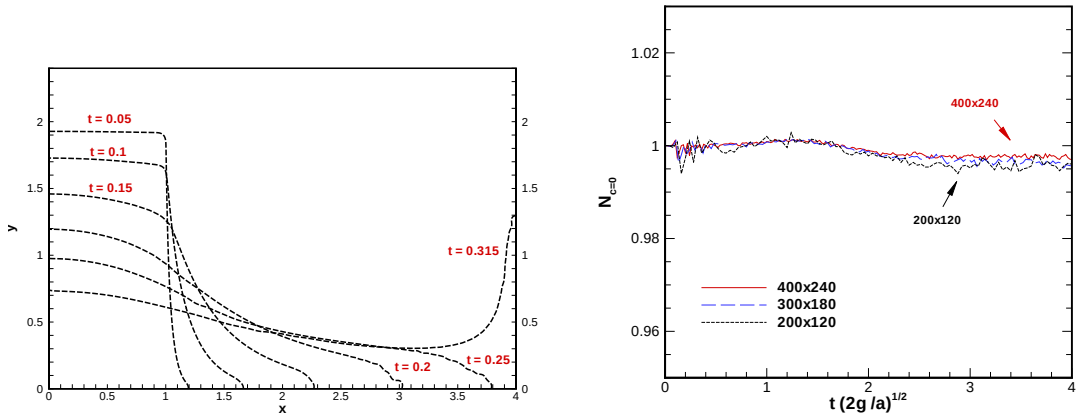

(a) (b)

Figure 5: (a) The time-history of the predicted free surface profiles for the dam-break problem in the domain of 400×240 mesh points; (b) The predicted area ratios $N_{c=0}$, defined in (5.1), are plotted with respect to time t for the calculations carried out in three grids.

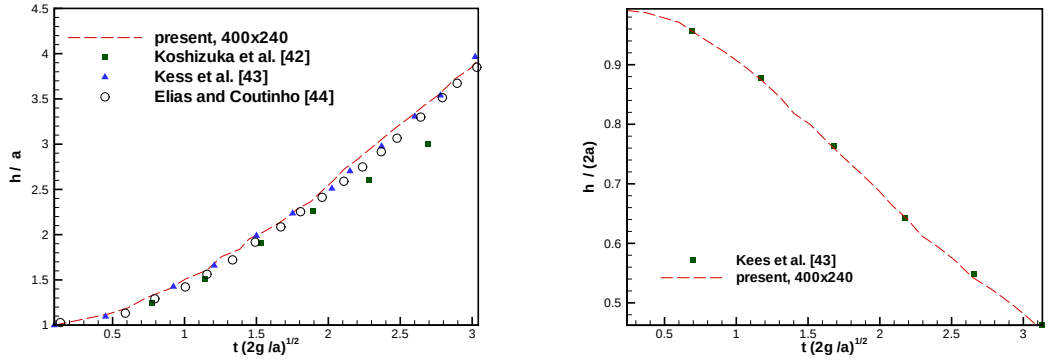

(a) (b)

Figure 6: Comparison of the predicted water heights with respect to time t.

6.1.2 Rayleigh-Taylor problem

The Rayleigh-Taylor instability arising from the penetration of a fluid into another lighter fluid along the direction of gravity has been studied in many scientific and environmental fields. The density difference is represented by the Atwood ratio $(\equiv(\rho_h-\rho_l)/(\rho_h+\rho_l))$. We validate our code by solving the same problem investigated in [8, 45, 46] at the Atwood ratio $=0.5$ and the viscosity ratio $=1.0$. The initial interface is located at $y(x)=-0.1D\cos(2\pi x/D)$ in a rectangular domain $[0,D]\times[-2D,2D]$.

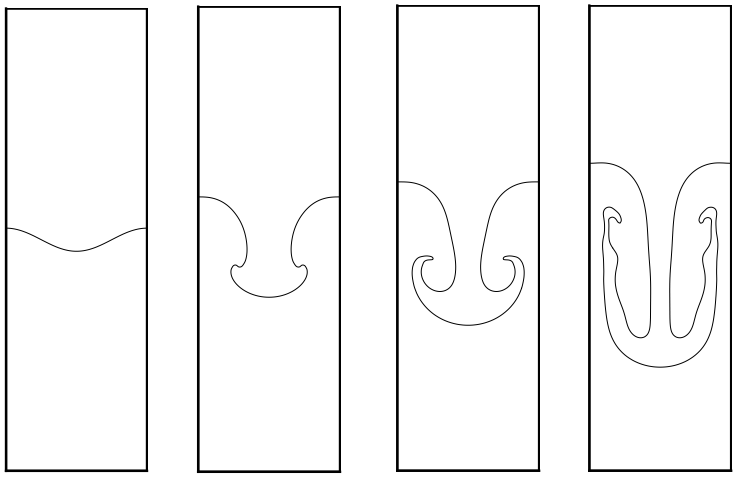

Figure 7: The time-evolving interfaces for the Rayleigh-Taylor instability problem predicted at different times. (a) $t=0.0$; (b) $t=1.25$; (c) $t=1.75$; (d) $t=2.5$.

The evolution of the interface investigated at $Re(\frac{\rho_h D^{3/2} g^{1/2}}{\mu})=3000$ is plotted in Fig. 7 at $t=0$,1.25,1.75, and 2.5. We also compare the upper rising fluid and the lower falling fluid with the solutions of Guermond and Quartapelle [46], and Ding et al. [8] in Fig. 8(a-b). The area ratios $N_{c=0}$ predicted in 100×400 and 200×800 two meshes are plotted in Fig. 8(c).

6.2 Interface prediction with surface tension

6.2.1 Bubble rising problem

The interface problem with the surface tension being considered is then investigated at the density ratio $\rho_G/\rho_L=0.0013$ and the viscosity ratio $\mu_G/\mu_L=0.016$. This problem is characterized by the Reynolds number Re=500, Weber number We=0.68, and the Froude number $Fr=0.45$. In the rectangle $[0,2]\times[0,4]$, the bubble at $t=0$ is a circle of radius 0.5 with its center located at $(1.0,1.0)$. No-slip boundary condition is imposed on the vertical and horizontal walls. The initial velocity is zero everywhere in the domain.

In Fig. 9, the free surfaces predicted in the domain of 100×200 and 200×400 nodal points are plotted at t= 0.5, 0.8 and 1.0. We can see from Fig. 9(a) that the results predicted from the UCCD7 scheme agree quite well with the results obtained by Olsson and Kreiss [20]. Also, Fig. 9(d) shows excellent area preservation property.

6.2.2 Three-dimensional two-bubble merging problem

Two spherical bubbles of the radius R $(=1)$ merging coaxially and obliquely in the domain of $[0,4R]\times[0,4R]\times[0,8R]$ will be investigated. For the coaxial bubble problem,

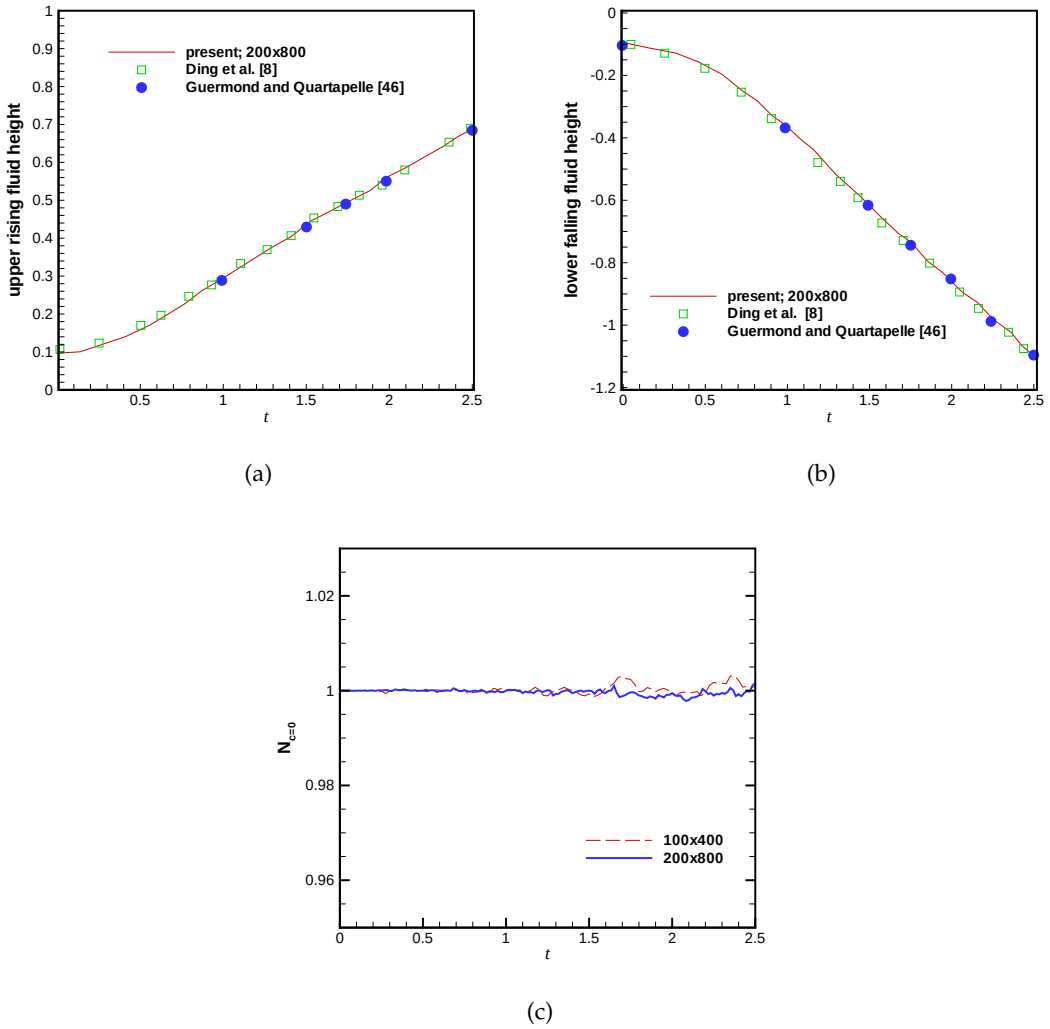

Figure 8: Comparison of the predicted time-varying upper rising fluid heights in (a) and the lower falling fluid height in (b); (c) The predicted area ratios $N_{c=0}$, defined in (5.1), are plotted with respect to time t for the calculations carried out in two grids.

the center of the upper bubble is at $(2R,2R,2.5R)$ and the center of the lower bubble is at $(2R,2R,1R)$. For the oblique bubble problem, the center of the upper bubble is $(2R,2R,2.5R)$ and the center of the lower bubble is $(2.85R,2R,1R)$. The physical properties are chosen as $Re=67.27$, $We=16$, and $Fr=1$, which are the same as those used in the experimental study by Brereton and Korotney [47].

Our computations are carried out in $80\times80\times160$ grids. The density and viscosity ratios are chosen to be $\rho_G/\rho_L=0.001$ and $\mu_G/\mu_L=0.01$, respectively. For the coaxial bubble problem, we only compare the interface profile at the $x-z$ midplane. Good agreement

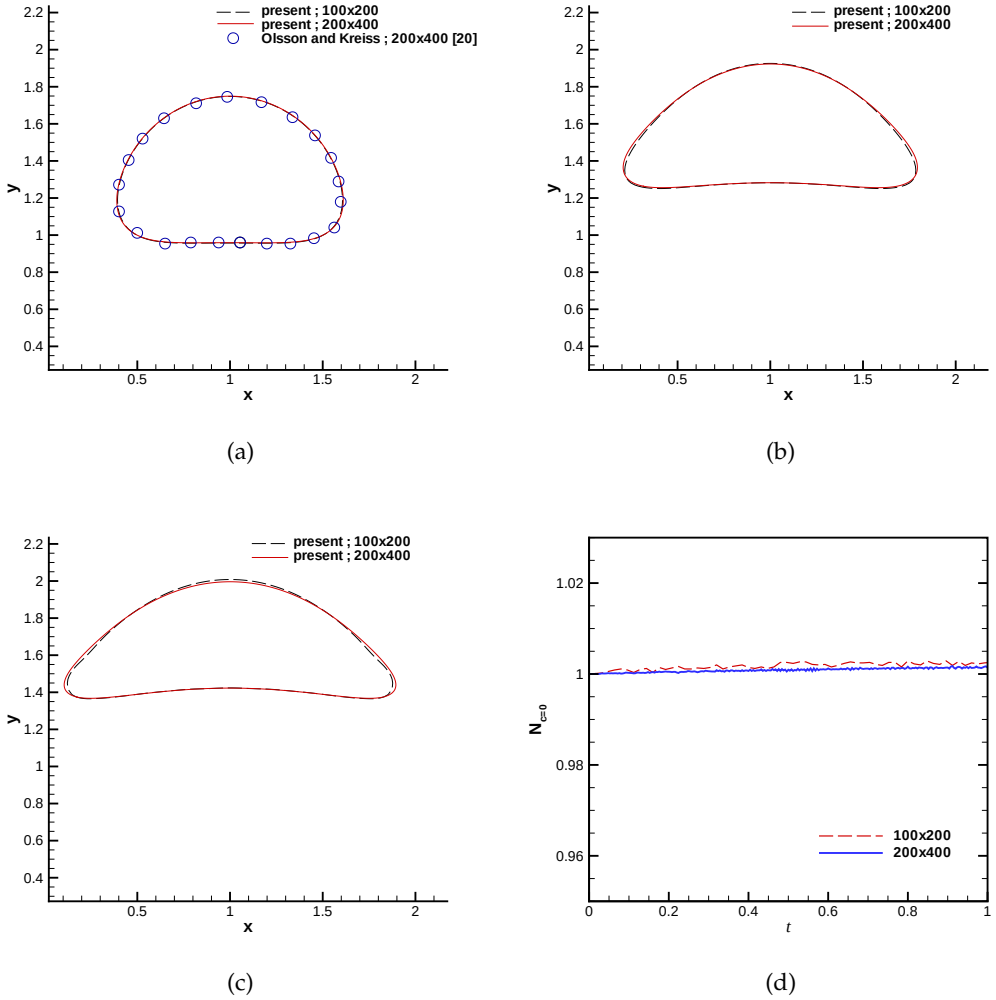

Figure 9: The time-evolving free surfaces for the bubble rising problem predicted at different times. (a) $t=0.5$; (b) $t=0.8$; (c) $t=1.0$; (d) The predicted area ratios $N_{c=0}$, defined in (5.1), are plotted versus t for the calculations carried out in 100×200 and 200×400 grids.

with the experimental observation by Brereton and Korotney [47] can be seen in Fig. 10. We also compare the oblique bubble problem with the numerical solutions of Chiu and Lin [48] in Fig. 11. For the sake of completeness, the values of $M_{c=0}$ are also plotted with respect to time in Fig. 12, showing again that the bubble volumes are well preserved for both the coaxial and oblique bubble rising cases.

6.2.3 Three-dimensional droplet falling in water problem

The droplet falling in water problem has been investigated by the authors in [48–51] in order to show the applicability of their proposed methods to simulate complex interface

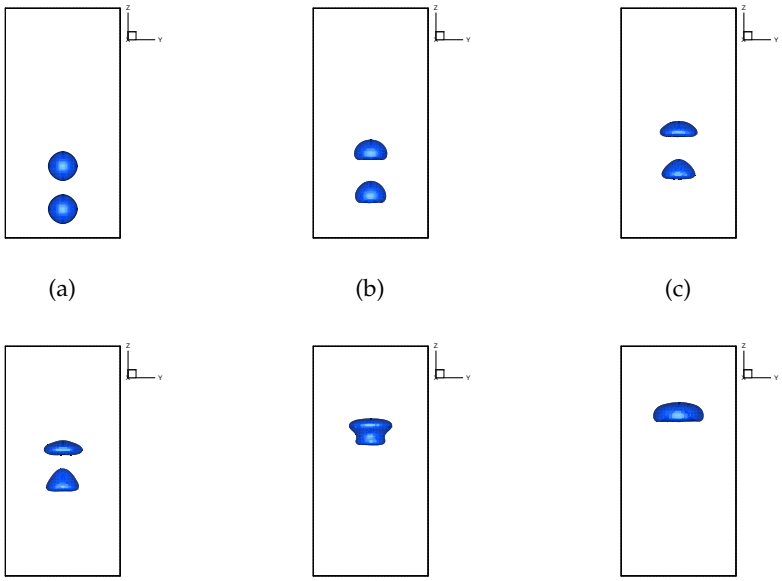

Figure 10: The time-evolving coaxial bubble problem predicted at different times. (a) $t=0.0s$; (b) $t=0.03s$; (c) $t=0.06s$; (d) $t=0.09s$; (e) $t=0.12s$; (f) $t=0.15s$.

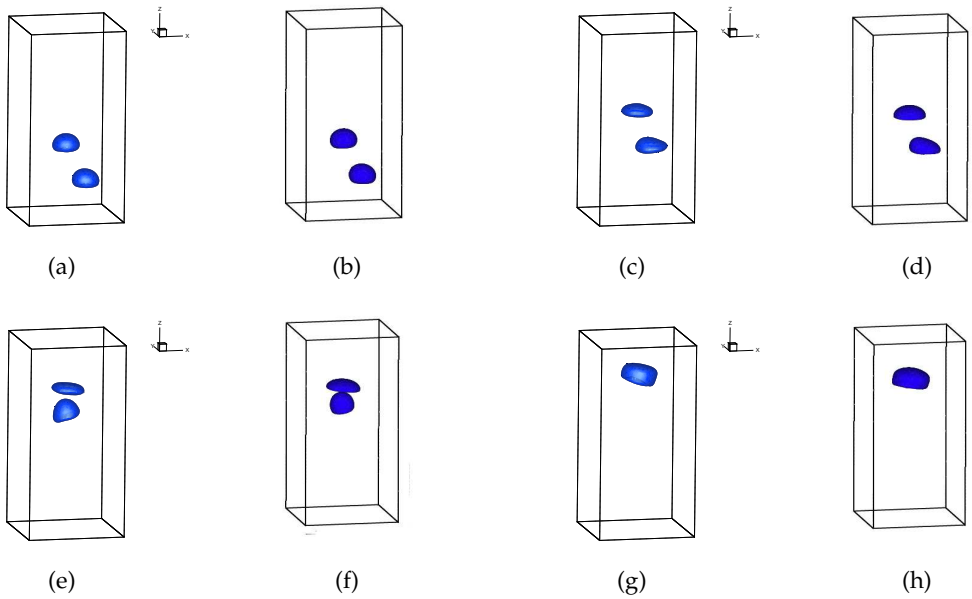

Figure 11: The time-evolving oblique bubble predicted at different times. (a) $t=0.03s$; (b) $t=0.03s$ [48]; (c) $t=0.09s$; (d) $t=0.09s$ [48]; (e) $t=0.15s$; (f) $t=0.15s$ [48]; (g) $t=0.18s$; (h) $t=0.18s$ [48].

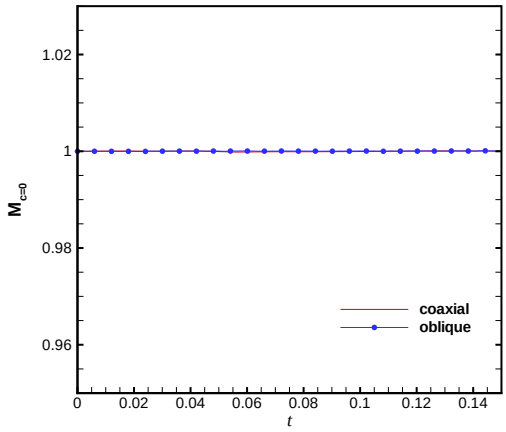

Figure 12: The predicted volume ratios, defined in (5.2), are plotted with respect to time t for the calculation carried out in $80\times80\times160$ grids.

formation resulting from the droplet falling into a thin liquid layer. The density ratio for the liquid and air is 0.001, and the viscosity ratio for the liquid and air is 0.01. The initial droplet diameter is $D=5.33mm$ and the depth of liquid layer is $1.0mm$. This droplet falls down with the velocity $20\frac{m}{s}$ into a liquid thin film of $1mm$ depth. Fig. 13 shows the result computed at $We=800$, $Re=600$, in $200\times200\times100$ grids. We also predict this problem at $We=200$, $Re=200$ (Fig. 14) and at $We=10$, $Re=200$ (Fig. 15). In this study,

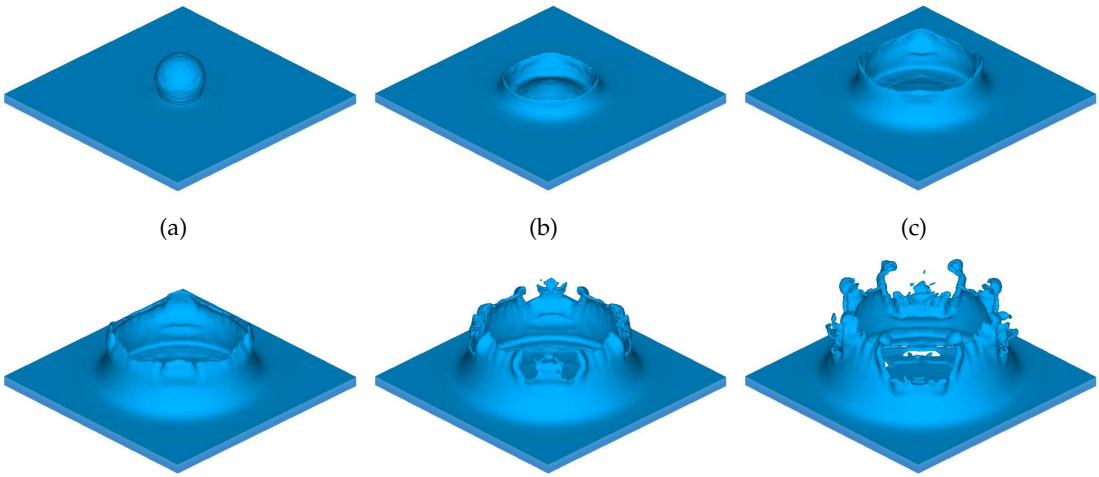

Figure 13: The time-evolving free surfaces predicted at different times with $We=800$ and $Re=600$ for the droplet falling in water problem. (a) t=0.024; (b) t=0.096; (c) t=0.168; (d) t=0.24; (e) t=0.312; (f) t=0.384.

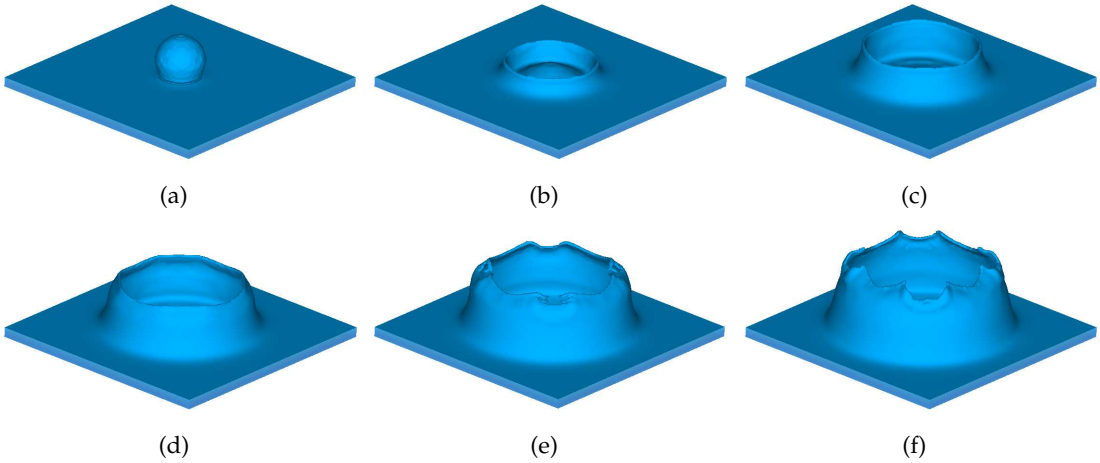

Figure 14: The time-evolving free surfaces predicted at different times with $We=200$ and $Re=200$ for the droplet falling in water problem. (a) $t=0.024$; (b) $t=0.096$; (c) $t=0.168$; (d) $t=0.24$; (e) $t=0.312$; (f) $t=0.384$.

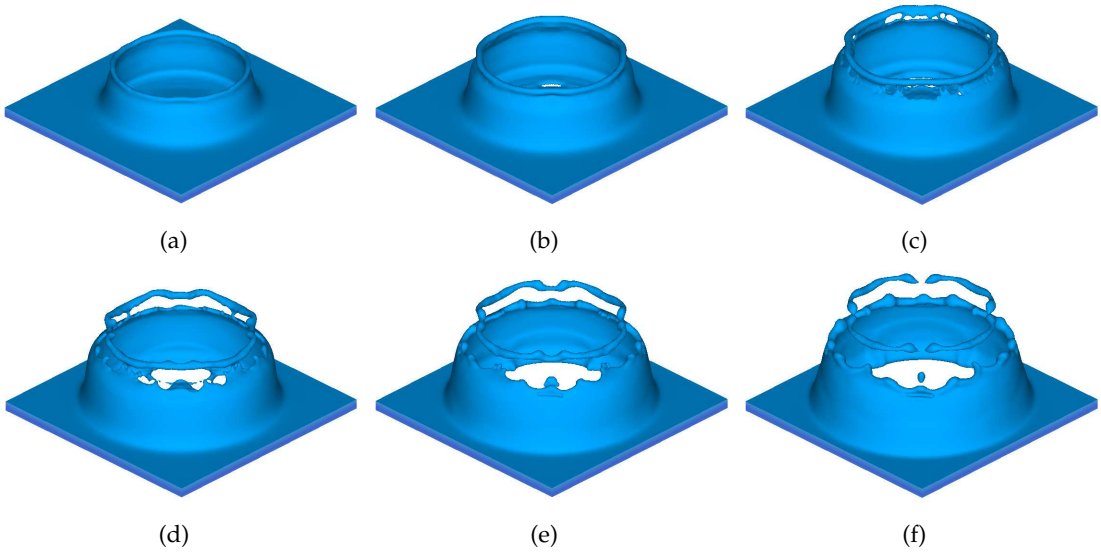

Figure 15: The time-evolving free surfaces predicted at different times with $We=10$ and $Re=200$ for the droplet falling in water problem. (a) $t=0.168$; (b) $t=0.24$; (c) $t=0.312$; (d) $t=0.384$; (e) $t=0.456$; (f) $t=0.528$.

the droplet splashing phenomenon may not be sharply predicted yet because the level set method applied to predict interface is known to suffer, more or less, the problem of non-conserved mass shown in Fig. 16. Most mass loss comes most likely from process of droplet splashing.

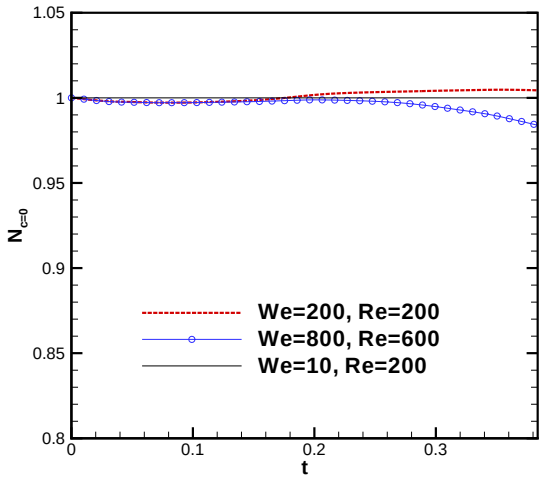

Figure 16: The predicted volume ratios, defined in (5.2), are plotted with respect to time t for the calculation carried out in $200\times200\times100$ grids.

7 Concluding remarks

This paper presents a numerical method to solve the incompressible Navier-Stokes equations and the level set equation in collocated grids. The interface is moved implicitly by the advection of level set function ϕ, which is split into two steps. First, ϕ is advected using the symplectic temporal scheme SRK6 and the spatial scheme UCCD7 with the minimized numerical phase error to preserve the mass conservation and capture interface excellently. Then the re-initialization step is performed to make sure ϕ as a distance function. For the verification purpose, the vortex flow in a box and the slotted (Zalesak's) disk problems are investigated. For the validation purpose, the coupled systems of hydrodynamic and level set equations for the dam-break, Rayleigh-Taylor, bubble rising, two-bubble merging, and droplet falling in water problems are also solved. All the predicted results for the problems with and without taking the surface tension into consideration have been shown to compare fairly well with their corresponding experimental or other numerical results.

Acknowledgments

This study was supported by NSC-97-2221-E-002-250-MY3 and Fundamental Research Funds for the Central Universities 2014QNA4030.

References

[1] C. W. Hirt, A. A. Amsden and J. L. Cook, An arbitrary Lagrangian-Eulerian computing method for all flow speeds, J. Comput. Phys., 135(2) (1997), 203-216.
[2] J. M. Boultone-Stone and J. R. Blake, Gas bubbles bursting at a free surface, J. Fluid Mech., 254 (1993), 437-466.
[3] J. P. Best, The formation of toroidal bubbles upon the collapse of transient cavities, J. Fluid Mech., 251 (1993), 79-107.
[4] Y. L. Zhang, K. S. Yeo, B. C. Khoo and C. Wang, 3D jet impact and toroidal bubbles, J. Comput. Phys., 166 (2001), 336-360.
[5] V. E. Badalassi, H. D. Ceniceros and S. Banerjee, Computation of multiphase systems with phase field models, J. Comput. Phys., 190 (2003), 371-397.
[6] J. Kim, A continuous surface tension force formulation for diffuse-interface models, J. Comput. Phys., 204 (2005), 784-804.
[7] J. Kim, Phase-field models for multi-component fluid flows, Commun. Comput. Phys., 12 (2012), 613-661.
[8] H. Ding, P. D. M. Spelt and C. Shu, Diffuse interface model for incompressible two-phase flows with large density ratios, J. Comput. Phys., 226 (2007), 2078-2095.
[9] C. W. Hirt and B. D. Nichols, Volume of fluid (VOF) method for the dynamics of free boundaries, J. Comput. Phys., 39 (1981), 201-225.
[10] S. Chen, D. B. Johnson and P. E. Raad, Velocity boundary conditions for the simulation of free surface fluid flow, J. Comput. Phys., 116 (1995), 262-276.
[11] R. Caiden, R. Fedkiw and C. Anderson, A numerical method for two phase flow consisting of separate compressible and incompressible regions, J. Comput. Phys., 166 (2001), 1-27.
[12] B. Li and J. Shopple, An interface-fitted finite element level set method with application to solidification and solvation, Commun. Comput. Phys., 10(1) (2011), 32-56.
[13] S. Osher and J. A. Sethian, Fronts propagating with curvature dependent speed: algorithms based on Hamilton-Jacobi formulations, J. Comput. Phys., 79 (1988), 12-49.
[14] M. Sussman and E. Fatemi, An efficient interface preserving level set redistancing algorithm and its application to interfacial incompressible fluid flow, SIAM J. Sci. Comput., 20 (1999), 1165-1191.
[15] M. Sussman, P. Smereka and S. Osher, A level set approach for computing solutions to incompressible two-phase flow, J. Comput. Phys., 114 (1994), 146-159.
[16] E. Marchandise, J. F. Remacle and N. Chevaugeon, A quadrature-free discontinuous Galerkin method for the level set equation, J. Comput. Phys., 212 (2006), 338-357.
[17] D. Enright, R. Fedkiw, J. Ferziger and I. Mitchell, A hybrid particle level set method for improved interface capturing, J. Comput. Phys., 183 (2002), 83-116.
[18] M. Sussman and E. G. Puckett, A coupled level set and volume-of-fluid method for computing 3D and axisymmetric incompressible two-phase flow, J. Comput. Phys., 162 (2000), 301-337.
[19] F. Losasso, R. Fedkiw and S. Osher, Spatially adaptive techniques for level set methods and incompressible flow, Comput. Fluids, 35 (2006), 995-1010.
[20] E. Olsson and G. Kreiss, A conservative level set method for two phase flow, J. Comput. Phys., 210 (2005), 225-246.
[21] S. Osher and R. Fedkiw, Level set methods: An overview and some recent results, J. Comput. Phys., 169 (2001), 463-502.
[22] S. Osher and R. Fedkiw, Level Set Methods and Dynamic Implicit Surfaces, Springer-Verlag:

Berlin, 2003.
[23] M. Sussman, E. Fatemi, P. Smereka and S. Osher, An improved level set method for incompressible two-phase flows, Comput. Fluids, 27 (1998), 663-680.
[24] J. Sethian, Level Set Methods and Fast Marching Methods, Cambridge University Press, Cambridge, U. K, 1999.
[25] J. A. Sethian, Evolution, implementation, and application of level set and fast marching methods for advancing fronts, J. Comput. Phys., 169 (2001), 503-555.
[26] P. J. Morrison, Hamiltonian description of the ideal fluid, Rev. Mod. Phys., 70(2) (1998), 467-521.
[27] T. G. Shepherd, A general method for finding extremal states of Hamiltonian dynamical systems, with applications to perfect fluids, J. Fluid Mech., 213 (1990), 573-587.
[28] R. I. McLachlan, Area preservation in computational fluid dynamics, Phys. Letter. A, 264 (1999), 36-44.
[29] C. K. W. Tam and J. C. Webb, Dispersion-relation-preserving finite difference schemes for computational acoustics, J. Comput. Phys., 107 (1993), 262-281.
[30] W. Oevel and M. Sofroniou, Symplectic Runge-Kutta schemes II: classification of symmetric method, Univ. of Paderborn, Germany, Preprint, 1997.
[31] G.-S. Jiang and D. Peng, Weighted ENO schemes for Hamilton-Jacobi equations, SIAM J. Sci. Comput., 21 (2000), 2126-2143.
[32] C. W. Shu and S. Osher, Efficient implementation of essentially non-oscillatory shock-capturing schemes, J. Comput. Phys., 77 (1988), 439-471.
[33] J. B. Bell, P. Colella, H. M. Glaz, A second-order projection method for the incompressible Navier-Stokes equations, J. Comput. Phys., 85 (1989), 257-283.
[34] T. W. H. Sheu and P. H. Chiu, A divergence-free-condition compensated method for incompressible Navier-Stokes equations, Comput. Methods Appl. Mech. Engrg., 196 (2007), 4479-4494.
[35] T. Nihei and K. Ishii, A fast solver of the shallow water equations on a sphere using a combined compact difference scheme, J. Comput. Phys., 187 (2003), 639-659.
[36] J. W. Kim and D. J. Lee, Optimized compact finite difference schemes with maximum resolution, AIAA J., 34(5) (1996), 887-893.
[37] P. C. Chu and C. Fan, A three-point combined compact difference scheme. J. Comput. Phys., 140 (1998), 370-399.
[38] R. Vichnevetsky and J. B. Bowles, Fourier Analysis of Numerical Approximations of Hyperbolic Equations, SIAM, Philadelphia, 1982.
[39] A. K. De and V. Eswaran, Analysis of a new high resolution upwind compact scheme, J. Comput. Phys., 218 (2006), 398-416.
[40] S. T. Zalesak, Fully multidimensional flux-corrected transport algorithms for fluids, J. Comput. Phys., 31 (1979), 335-362.
[41] Z. Wang, J. Yang, B. Koo and F. Stern, A coupled level set and volume-of-fluid method for sharp interface simulation of plunging breaking waves, Int. J. Multiphase Flows, 35 (2009), 227-246.
[42] S. Koshizuka, H. Tamako and Y. Oka, A particle method for incompressible viscous flow with fluid fragmentation, Comput. Fluid Mech. J., 113 (1995), 134-147.
[43] C. E. Kees, I. Akkerman, M. W. Farthing and Y. Bazilevs, A conservative level set method suitable for variable-order approximations and unstructured meshes, J. Comput. Phys., 230 (2011), 4536-4558.
[44] R. N. Elias and A. L. G. A. Coutinho, Stabilized edge-based finite element simulation of

free-surface flows, Int. J. Numer. Meth. Fluids, 54 (2007), 965-993.
[45] G. Tryggvason, Numerical simulations of the Rayleigh-Taylor instability, J. Comput. Phys., 75 (1988), 253-382.
[46] J. -L. Guermond and L. Quartapelle, A projection FEM for variable density incompressible flows, J. Comput. Phys., 165 (2000), 167-188.
[47] G. Brereton and D. Korotney, Coaxial and oblique coalescence of two rising bubbles, in: I. Sahin, G. Tryggvason (Eds.), Dynamics of Bubbles and Vortices Near a Free Surface, MD-Vol. 119, ASME, New York, 1991.
[48] P. H. Chiu and Y. T. Lin, A conservative phase field method for solving incompressible two-phase flows, J. Comput. Phys., 230 (2011), 185-204.
[49] M. Rieber and A. Frohn, A numerical study on the mechanism of splashing, Int. J. Heat Fluid Flow, 20 (1999), 455-461.
[50] F. Xiao, A. Ikebata and T. Hasegawa, Numerical simulations of free-interface fluids by a multi integrated moment method, Comput. Struct., 83 (2005), 409-423.
[51] K. Yokoi, A numerical method for free-surface flows and its application to droplet impact on a thin liquid layer, J. Sci. Comput., 35 (2008), 372-396.